—MAE Independent Senior Design Project— Modeling, Design, and Autonomous Control of a Single Motor Glider

Robert Whitney - rw429@cornell.edu

Spring 2020

Contents

1 Introduction

1.1 Motivation

The purpose of this report is to record the modeling and control system design for a single motor remote control airplane, with the intended goal of the project being a robust and fully autonomous system. Motivation for undertaking the project comes from a desire to continue developing practical design skills, supplement course work on feedback and control system design, and to establish a working proficiency with different industry design and simulation tools.

A commercial autopilot is a necessary tool for industries planning on using Unmanned Aerial Vehicles (UAVs) frequently. Any UAV is a highly complicated dynamical system that takes either costly professional experience or extensive training to pilot effectively. The cost associated with human operators may be avoided by developing a robust controller that can regulate the UAV and ensure safety and the completion of the mission.

A commercial autopilot for small UAVs has a myriad of applications across several industries.

- Agriculture : crop surveillance, assisted pollination
- Entertainment : multi-aircraft demonstrations, cinematography
- Land surveying and inspection
- Emergency response : search and rescue, aerial vantage point
- Security

Compared to multi-rotor platforms, fixed-wing UAVs are faster and more efficient at the cost of maneuverability and vertical take off and landing. Thus, fixed-wing UAVs are suited to missions that require increased range, operating time, or payload capacity. A fixed-wing UAV was chosen in this project over a multi-rotor because of a lack of experience with fixed-wing UAVs.

1.2 Aerodynamic Nomenclature

	Roll (X)	Pitch (Y)	Yaw (Z)
Linear Velocity	u	v	w
Angular Velocity	p	q	r
Aerodynamic Force	D	Y	L
Aerodynamic Moment	l	m	n

2 System Model

2.1 Reference Frames and Attitude Representation

Analysis begins with defining the necessary reference frames. Each reference frames consist of 3 unit-length orthogonal vectors and are illustrated in *Figure 1.*

- $\mathcal{I} = \{\hat{N}, \hat{E}, \hat{D}\}$ represents the Earth-fixed North-East-Down (NED) inertial frame. $\hat{N}$ points towards magnetic north, $\hat{D}$ points in the direction of gravity, and $\hat{E}$ points east, parallel to the ground such that $\hat{D} \times \hat{N} = \hat{E}$.

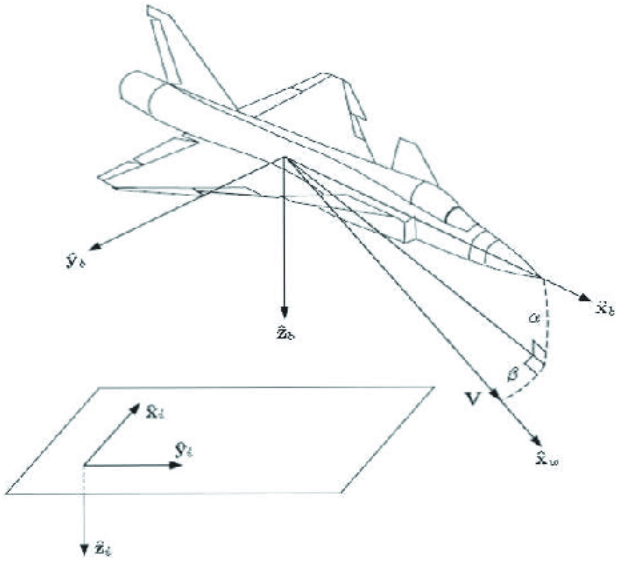

Figure 1: The inertial, body-fixed, and wind-fixed reference frames [3]

- $\mathcal{B} = \{\hat{X}_\mathcal{B}, \hat{Y}_\mathcal{B}, \hat{Z}_\mathcal{B}\}$ represents the body-fixed frame whose origin is located at the center of mass of the aircraft. $\hat{X}_\mathcal{B}$ points out the nose, $\hat{Y}_\mathcal{B}$ points towards the starboard wing, and $\hat{Z}_\mathcal{B}$ points out the belly of the aircraft.
- $\mathcal{W} = \{\hat{X}_W, \hat{Y}_W, \hat{Z}_W\}$ represents the wind-fixed frame whose origin is located at the center of mass of the aircraft. $\hat{X}_\mathcal{W}$ points in the direction of the velocity vector of the aircraft relative to the air, $\hat{Z}_\mathcal{W}$ points in the plane of symmetry of the aircraft out the belly, and $\hat{Y}_\mathcal{W}$ points such that $\hat{Z}_\mathcal{W} \times \hat{X}_\mathcal{W} = \hat{Y}_\mathcal{W}$.

A 3-2-1 Euler angle sequence is used to represent the attitude of $\mathcal{B}$ with respect to $\mathcal{I}$ (*Figure 2*). The transition is defined by

1. ... a rotation about $\hat{D}$ by ψ (yaw)
2. ... a rotation about $\hat{E}$' by θ (pitch) where $\hat{E}$ has been rotated by ψ to produce $\hat{E}$'
3. ... and a rotation about $\hat{N}$" by ϕ (roll) where $\hat{N}$ has been rotated by ψ and θ appropriately.

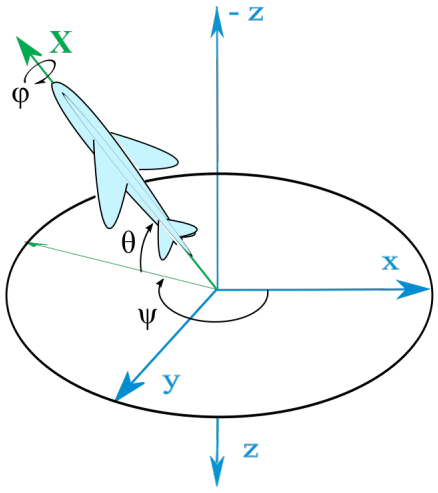

Figure 2: A transformation from the inertial frame to the body-fixed frame [15].

To transition between $\mathcal{W}$ and $\mathcal{B}$, two additional angles are defined (*Figure 3*) [8]. The angle of attack α is the angle between $\hat{X}_{\mathcal{B}}$ and $\hat{X}_{\mathcal{W}}$ projected onto the *vertical* plane of symmetry of the aircraft while the sideslip angle β is the angle between $\hat{X}_{\mathcal{B}}$ and $\hat{X}_{\mathcal{W}}$ projected onto the *horizontal* plane of symmetry. The aircraft *points* along $\hat{X}_{\mathcal{B}}$, but *moves* along $\hat{X}_{\mathcal{W}}$. A set of Euler angles (μ, γ, χ) represents the attitude of $\mathcal{W}$ with respect to $\mathcal{I}$.

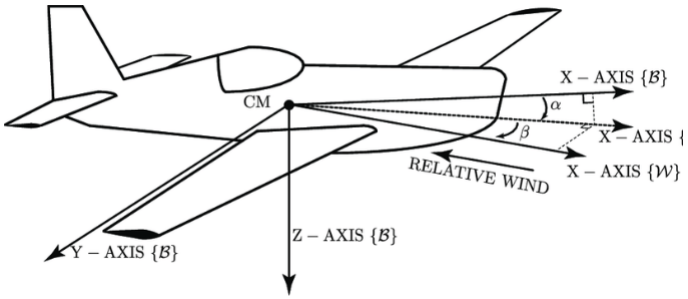

Figure 3: A transformation between the wind frame and the body frame [9].

2.2 Equations of Motion

The translational dynamics are given by a linear momentum balance in the body-fixed frame [10]. The equation includes the velocity vector $\vec{V_{\mathcal{B}}}$, the sum of the aerodynamic forces $\sum \vec{F}_{\mathcal{B},Aero}$, the mass m, a rotation matrix $R_{\mathcal{I}\to\mathcal{B}}$, the gravity vector in the inertial frame $\vec{g_{\mathcal{I}}}$, and the skew-symmetric matrix $\widetilde{\omega}_{\mathcal{B}}$.

$$\frac{\partial \vec{V_{\mathcal{B}}}}{\partial t} = \frac{\sum \vec{F}_{\mathcal{B},Aero}}{m} + R_{\mathcal{I}\to\mathcal{B}} \cdot \vec{g_{\mathcal{I}}} - \widetilde{\omega}_{\mathcal{B}} \vec{V_{\mathcal{B}}}$$

$$\widetilde{\omega}_{\mathcal{B}} = \begin{bmatrix} 0 & -\omega_Z & \omega_Y \\ \omega_Z & 0 & -\omega_X \\ -\omega_Y & \omega_X & 0 \end{bmatrix}$$

The rotational dynamics are given by an angular momentum balance in the body-fixed frame [10]. The equation includes the angular velocity vector $\vec{\omega}_{\mathcal{B}}$, the moment of inertia $I_{\mathcal{B}}$, and the sum of the moments due to aerodynamics $\sum \vec{M}_{\mathcal{B},Aero}$. The off-diagonal components of $I_{\mathcal{B}}$ are assumed to be ≈ 0 because of the symmetry of the aircraft.

$$\frac{\partial \vec{\omega}_{\mathcal{B}}}{\partial t} = I_{\mathcal{B}}^{-1}(\sum \vec{M}_{\mathcal{B},Aero} - \widetilde{\omega}_{\mathcal{B}} I_{\mathcal{B}} \vec{\omega}_{\mathcal{B}})$$

$$I_B = \begin{bmatrix} I_{xx} & -I_{xy} & -I_{xz} \\ -I_{xy} & I_{yy} & -I_{yz} \\ -I_{xz} & -I_{yz} & I_{zz} \end{bmatrix}$$

2.3 Aerodynamic Coefficients and Stability Derivatives

To solve for the complicated effects of aerodynamics, a popular approach in the literature is to define a non-dimensional coefficient that relates the total force on an object to the density of the fluid ρ, an appropriate reference area A, the velocity of the fluid V, and the coefficient C_{Aero} itself [1].

$$F_{Aero} = C \times \frac{1}{2}\rho A V^2$$

The total moment due to aerodynamics can be expressed in similar terms with the inclusion of an additional reference length l.

$$M_{Aero} = Cl \times \frac{1}{2}\rho A V^2$$

C_{Aero} can vary with the speed, viscosity, flow direction, and object size, among other parameters. To simplify the expression for C_{Aero}, two critical assumptions are made.

First, C_{Aero} is assumed to be a function of only the angle of attack α and control surface deflection δ. Under this assumption, C_{Aero} can be expressed as a Taylor Series expansion to help provide critical insight into the second assumption. In the second assumption, α and δ are assumed to be small. Under this assumption, the higher order terms in $C_{Aero}(\alpha, \delta)$ become sufficiently small to ignore.

$$C_{Aero} \approx C_{Aero}(\alpha, \delta)$$

$$C_{Aero}(\alpha,\delta) = f(c) + f'(c)(x-c) + \frac{f''(c)}{2!}(x-c)^2 + \frac{f'''(c)}{3!}(x-c)^3 + ... = \sum_{k=0}^{\infty} \frac{1}{k!} f^{(k)}(x)(x-c)^k$$

$$C_{Aero}(\alpha, \delta) \approx C_0(\delta) + C_\alpha \alpha$$

Since these assumptions are only valid near the operating point for which $C_{Aero}(\alpha, \delta)$ was calculated, stability derivatives are introduced to describe the change in C_{Aero} when there is a change in a flight condition parameter such as airspeed or angular velocity. In this system, the stability derivatives analyzed are those that relate the angular velocity to the moment about each axis (denoted by C_{a_b} for axis a and angular rate b).

$\sum \vec{F}_{\mathcal{B},Aero}$ and $\sum \vec{M}_{\mathcal{B},Aero}$ incorporate the appropriate aerodynamic coefficients and stability derivatives. In the equations below, δ_e and δ_r represent the elevator and rudder deflection, A represents the wing planform, $q_{dyn} = \frac{1}{2}\rho V^2$ represents the dynamic pressure, b and c represent the span and chord of the wing, C_{l_p} and C_{l_r} represent the roll damping due to roll and yaw rate, C_{m_q} represents the pitch damping due to pitch rate, and C_{n_p} and C_{n_r} represent the yaw damping due to roll and yaw rate.

$$F_{x,Aero} = F_{Drag} + F_{throttle} = C_D(\alpha, \delta_e)A \cdot q_{dyn} + F_{throttle}$$
$$F_{y,Aero} = F_{Side} = C_Y(\beta, \delta_r)A \cdot q_{dyn}$$
$$F_{z,Aero} = F_{Lift} = C_L(\alpha, \delta_e)A \cdot q_{dyn}$$

$$M_{x,Aero} = (C_l(\beta, \delta_r) + \frac{b}{2V}(C_{l_p}p + C_{l_r}r))A \cdot q_{dyn}$$
$$M_{y,Aero} = (C_m(\alpha, \delta_e) + \frac{c}{2V}C_{m_q}q)A \cdot q_{dyn}$$
$$M_{z,Aero} = (C_n(\beta, \delta_r) + \frac{bp}{2V}(C_{n_p}p + C_{n_r}r))A \cdot q_{dyn}$$

2.4 Throttle Model

A simple model of the throttle control input provides thrust for the aircraft. The relationship between percent throttle input and thrust is roughly linear.

$$F_{throttle} \approx C_{throttle}\delta_t, \qquad \delta_t \in [0, 1]$$

2.5 Longitudinal and Lateral Dynamics

The aircraft's 5 open-loop modes of motion can be classified as either longitudinal (3 Degrees of Freedom, motion along $\hat{X}_\mathcal{B}$ and $\hat{Z}_\mathcal{B}$, rotation about $\hat{Y}_\mathcal{B}$) or lateral (3 Degrees of Freedom, motion along $\hat{Y}_\mathcal{B}$, rotation about $\hat{X}_\mathcal{B}$ and $\hat{Z}_\mathcal{B}$) [12].

1. Short Period Mode (Longitudinal, Second Order) is characterized by highly damped pitching oscillations about the center of mass. The behavior of this mode is driven by the stiffness of the slope of $C_m(\alpha, \delta_e)$ and the value of C_{m_q}. The time for the amplitude to halve is on the order of 1-2 seconds.

2. Phugoid Mode (Longitudinal, Second Order) is slower decaying mode of the two longitudinal modes, characterized by a lightly damped exchange between gravitational potential and kinetic energy at constant α. It usually takes 10 times as long as the short period mode for the amplitude to decay by half. As a result, the phugoid mode dominates the aircraft's longitudinal trajectory.

3. Dutch Roll Mode (Lateral, Second Order) is a lightly damped exchange between roll and yaw oscillations, offset in phase by 90°. The time for the amplitude to halve is on the order of the short period mode. The time constant of the Dutch roll mode is similar to that of the short period mode.

4. Spiral Mode (Lateral, First Order) is characterized by a slow spiralling dive initiated by a small yaw or heading disturbance. Although this mode is generally unstable, the time for the amplitude to double is large enough to correct for the disturbance before entering the dive.

5. Roll Damping Mode (Lateral, First Order) is the most heavily damped of the lateral modes, characterized by a delay between when a roll is commanded and when the desired roll rate is achieve. Since it is heavily damped, the time to half the amplitude is small.

The 8 eigenvalues (6 oscillatory, 2 exponential) of the natural modes of motion define the open-loop stability of the aircraft. Thus, the characteristics of the open-loop modes are closely tied to how a controller is designed to achieve robust closed-loop stability.

2.6 Disturbance Model

A horizontal wind gust model was implemented to test the stability margins of the closed-loop system. The gust is modeled as an additional source of wind in the $\hat{N} \times \hat{E}$ plane with constant heading. The magnitude of the gust is variable over time, as shown in *Figure 27*.

The velocity vector of the wind is rotated to the body-fixed frame and added to the wind velocity vector due to the aircraft's motion in the inertial frame. Thus, the aircraft will experience a combination of a head-, tail-, and cross-wind depending on the orientation of the aircraft and the gust's heading.

3 Airframe Analysis and Design in Simulation

3.1 XFLR5

XFLR5, an airfoil analysis tool for low Reynolds number fluid flow, was used to estimate the aerodynamic coefficients and stability derivatives [11]. The original airframe was designed by the *Flite Test* community who offer free designs for simple foam board airplanes.

Figure 4: The *FT Simple Soarer* from the *Flite Test* community. The version pictured is an unpowered glider [13].

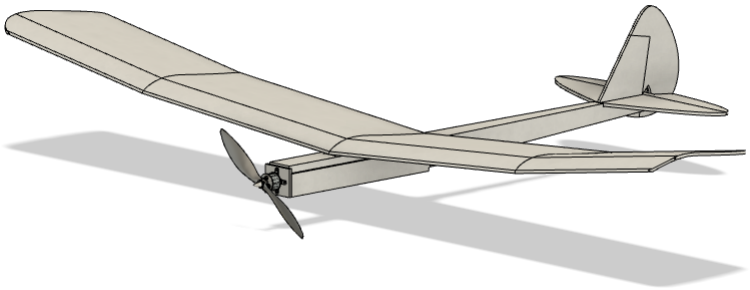

Figure 5: A CAD model of the aircraft

Using a CAD model as a guide (*Figure 5*), the camber and thickness of the airfoils were approximated in *XFLR5* (*Figures 6-7*). The aerodynamic coefficients of each airfoil were determined separately using the *Direct Airfoil Analysis* tool for $\alpha \in [-5, 15]$ and $Re \in [3 \times 10^4, 3 \times 10^6]$.

An airframe mesh was defined using the *Wing and Plane Design* tool which closely resembled the size, position, dihedreal, chord, span, mass, and orientation of the wing and control surfaces in the CAD model (*Figure 8*). Additional point masses were included in the aircraft to represent the battery, motor, servos, fuselage, and flight computer.

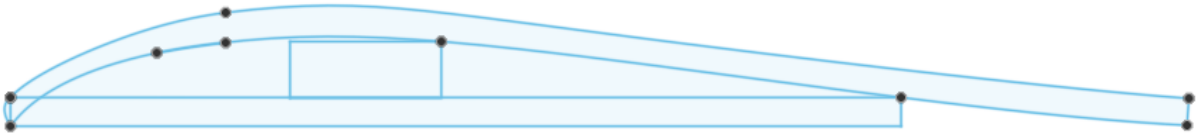

Figure 6: CAD model of the main airfoil

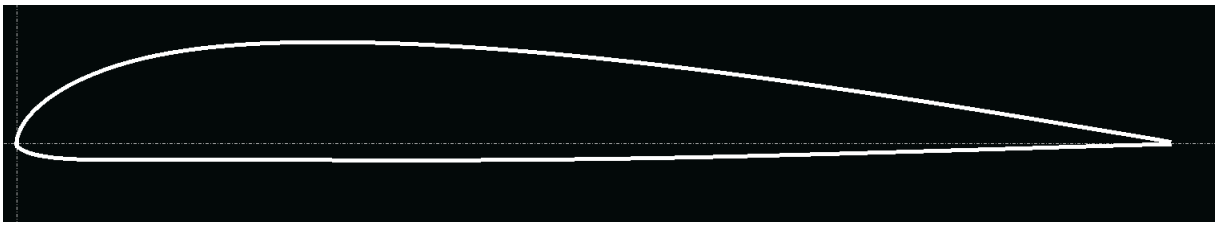

Figure 7: Approximation of main airfoil in *XFLR5*

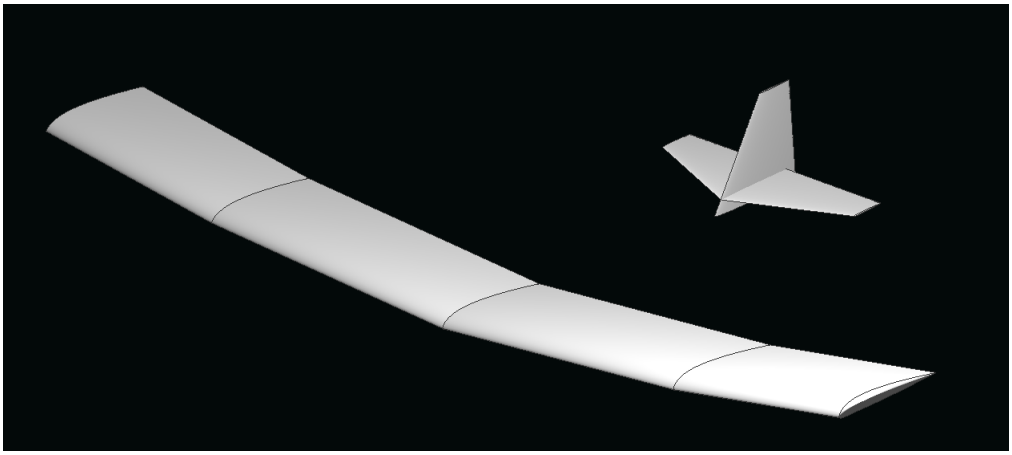

Figure 8: The wing, elevator, and fin models in *XFLR5*

Finally, an analysis was defined to solve for the total aerodynamic coefficients and stability derivatives at an operating point defined by $V_{air} = 10m/s, \rho = 1.21m/kg^3, \nu = 1.5 \times 10^{-5}m^2/s$ for a range of $\alpha \in [0°, 10°]$, $\beta \in [-5°, 5°]$ and for each combination of control surface deflection [12]. *Figure 9* shows the results of one such analysis.

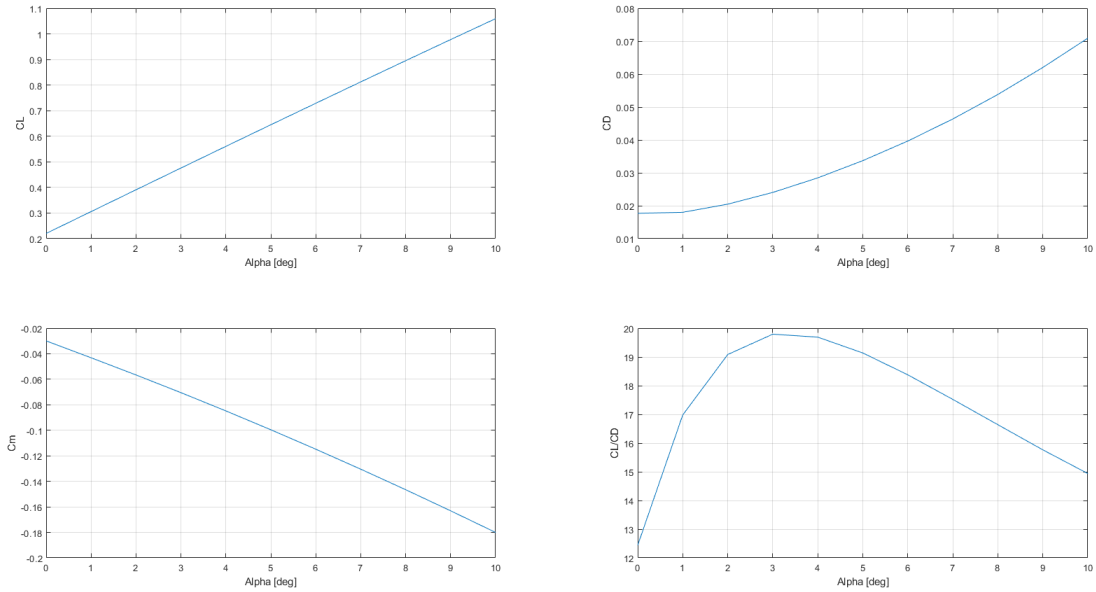

Figure 9: CL, CD, Cm, and CL/CD results from *XFLR5*

3.2 Airframe Design for Improved Longitudinal Stability

Improving open-loop stability reduces the effort the controller must exert to track a reference command in the presence of disturbances.

Center of mass placement is crucial for longitudinal stability. There only exists a stable equilibrium point α_{eq} when the slope of Cm vs. α is negative (*Figure 10*). In this case, when α increases due to disturbances, the pitching moment decreases and returns the plane to α_{eq}. Conversely, when α decreases, the pitching moment increases, also returning the plane to α_{eq}.

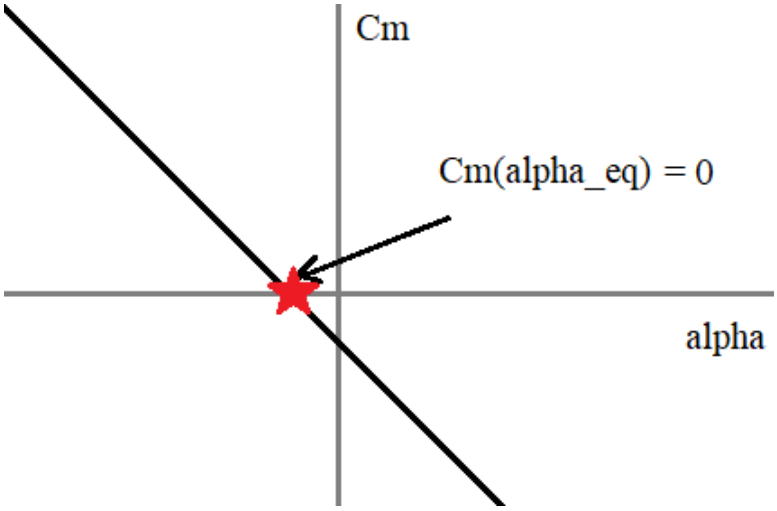

Figure 10: A plot of a stable Cm vs. α. Note that Cm(α_{eq})=0.

Moving the center of mass forward increases the longitudinal stability of the aircraft (the slope of Cm vs. α will steepen), but α_{eq} will decrease. The center of mass cannot be too far forward such that $CL(\alpha_{eq}) \leq 0$, otherwise the plane will not produce positive lift at its equilibrium point. If the center of mass is too far aft, the aircraft will be unstable (α_{eq} will be an *unstable* equilibrium point). A suitable position for the center of mass is 20-25% of the chord *aft* of the leading edge of the main airfoil.

4 Simulink Simulations

4.1 3 DoF Plant Simulation and PID Controller Design

A set of 3 Degree of Freedom (DoF) simulations were developed to analyze the longitudinal dynamics and validate the analysis methods before implementing a set of full 6 DoF simulations. All simulations were developed in *Simulink* using the *Aerospace Blockset* and *Aerospace Toolbox* to accelerate implementation [5] [6].

First, the longitudinal aerodynamic coefficients were interpolated using α and δ_e (*Figure 11*).

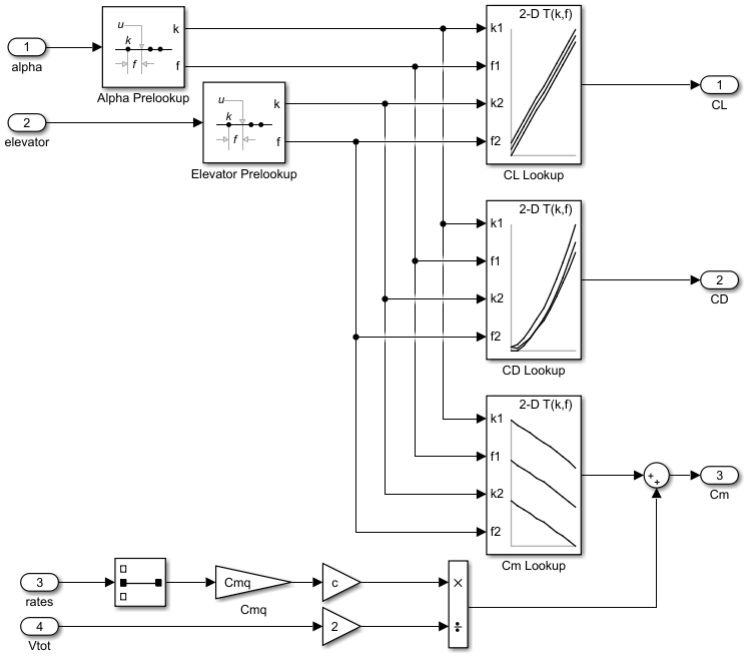

Figure 11: Interpolating the longitudinal aerodynamic coefficients using look-up tables for CL, CD, and Cm from *XFLR5*.

Next, the aerodynamic forces and moments were calculated using the dynamic pressure at the current speed and altitude (*Figure 12*).

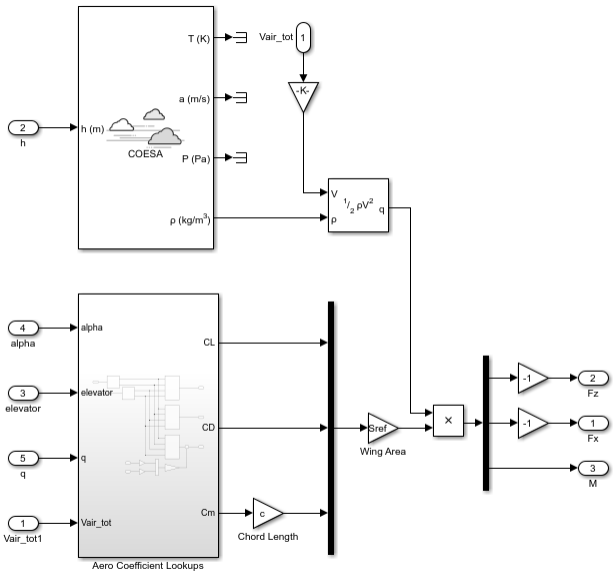

Figure 12: Calculating lift, drag, and pitching moment using the current dynamic pressure

To finish the 3 DoF model, the forces and moments were integrated in the wind axes to determine position, orientation, and velocity for each time-step until the stop time was reached (*Figure 13*). A non-linear second-order actuator block was used to model the elevator dynamics. An open-loop simulation of this model is shown in *Figure 14*. No disturbance model was implemented in the 3 DoF model.

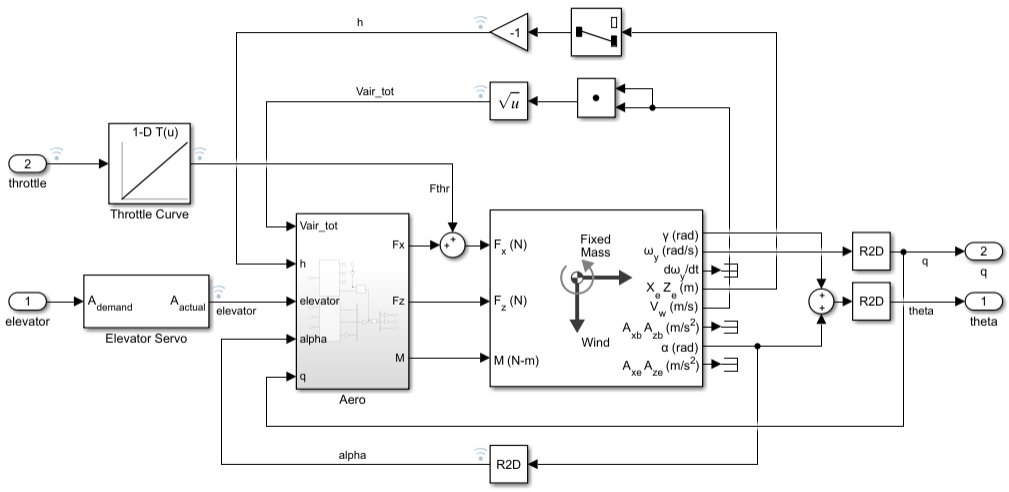

Figure 13: Integrating the equations of motion in the wind axes in the 3 DoF model

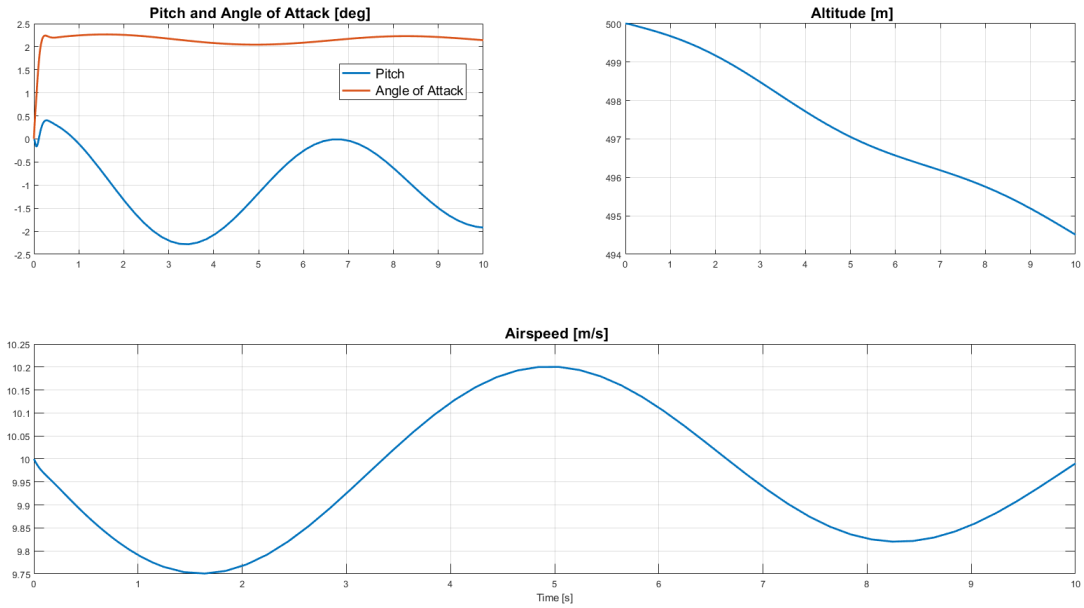

Figure 14: Open-Loop simulation of 3 DoF model.

The *MATLAB Linearization Manager* was used to find operating points for a glide slope of -15° at zero throttle and for steady level flight ($\gamma = 0°$) with non-zero throttle. Each operating point is determined by specifying steady-state constraints for some states

and solving for the unconstrained states. An operating point is used as a reference for controllers to stabilize towards.

A Proportional-Integral-Derivative (PID) controller was implemented to stabilize the aircraft to the operating point for steady flight [4]. It works by first calculating the error between the current output and a desired reference.

$$e(t) = y_{ref}(t) - y(t)$$

The control input is determined by taking the weighted sum of the error, its time-integral, and its time-derivative. Each weighting term K_p, K_i, K_d can be configured to achieve the desired performance and stability of the closed-loop system.

$$u(t) = K_p * e(t) + K_i \int_0^t e(\tau)d\tau + K_d\dot{e}(t)$$

After experimenting with different PID controller designs, a cascading PID controller that stabilizes the pitch and pitch rate controlled the aircraft with a desirable stability margin. The goal pitch rate is decided by a P controller ($K_i = 0, K_d = 0$) whereas the goal elevator deflection is decided by a PI controller ($K_d = 0$). *Figure 15* shows the structure of the controller in *Simulink*.

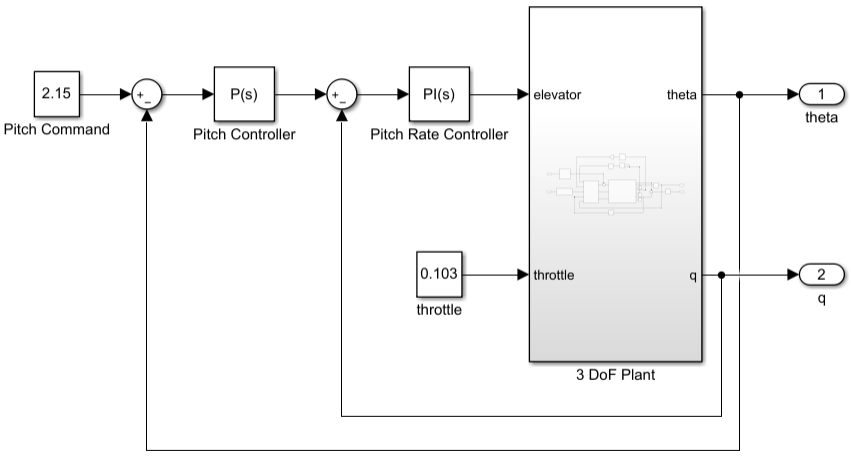

Figure 15: A cascading PID controller for pitch stabilization in the 3 DoF model

Figures 16-17 show the states of the aircraft tracking the operating point for steady level flight.

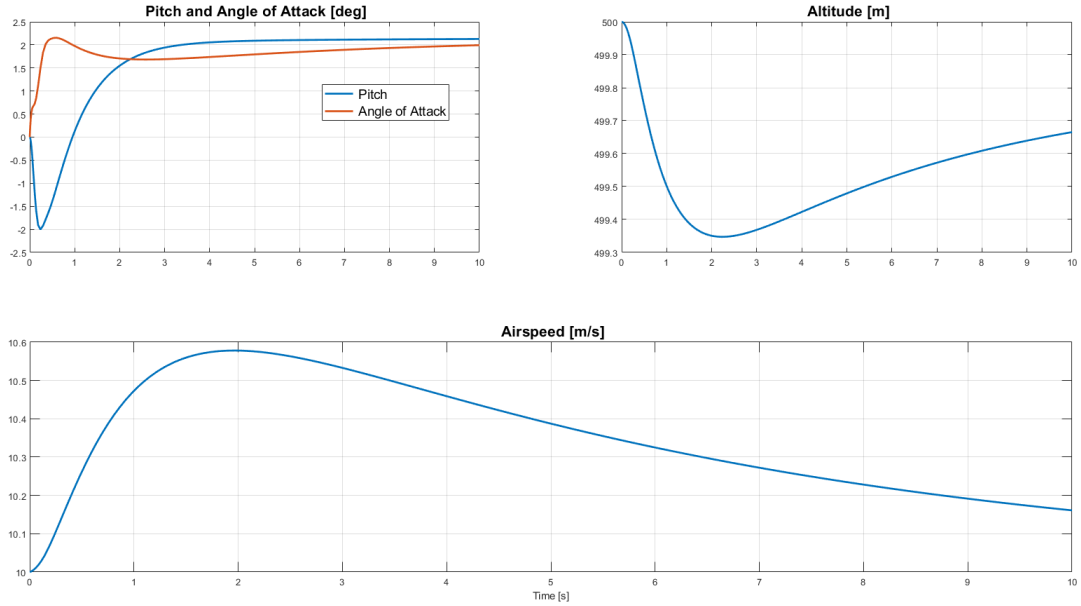

Figure 16: Using a PID controller to stabilize the 3 DoF model.

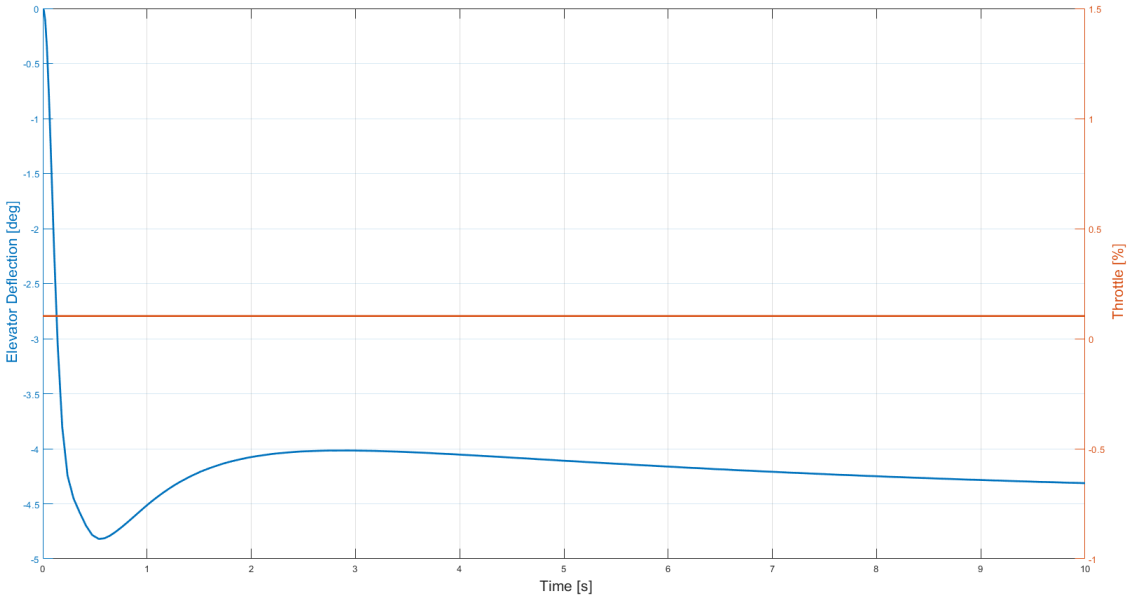

Figure 17: Control usage while using a PID controller in the 3 DoF model. Throttle input was set to a constant.

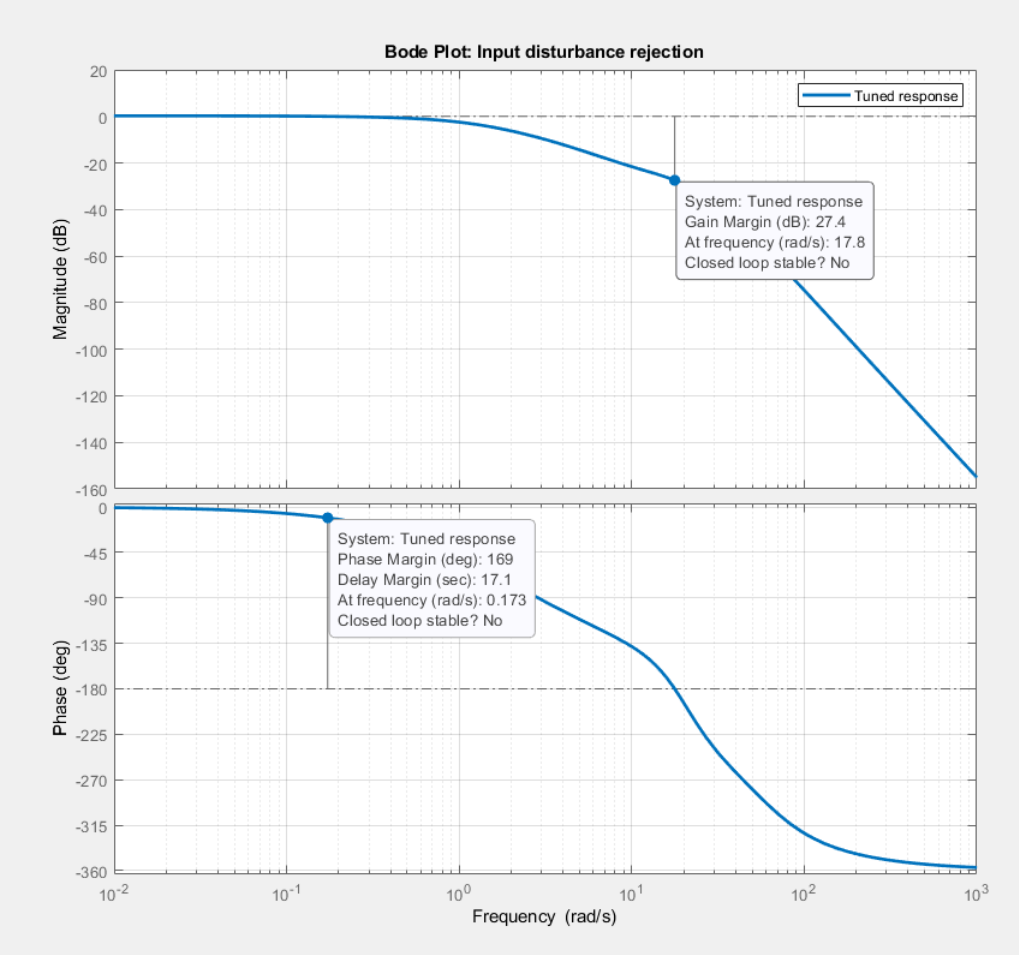

Figure 18: Frequency response for input disturbances in the 3 DoF model. Note that the label says there is not closed-loop stability because there is a zero at the origin.

4.2 6 DoF Plant Simulation and Controller Design

The 6 DoF model was developed using the 3 DoF model as a reference. The lateral aerodynamic coefficients were interpolated separately using sideslip β and rudder deflection δ_r. Again, the aerodynamic forces and moments were calculated using the dynamic pressure at the current speed and altitude (*Figure 19*).

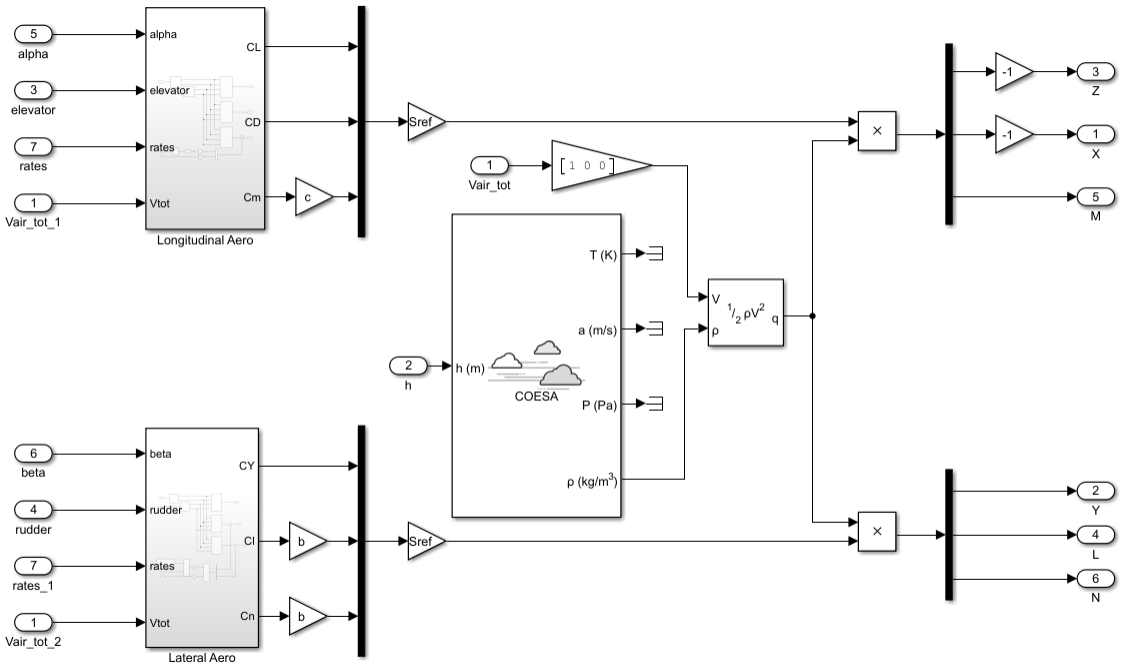

Figure 19: Calculating the forces and moments in the 6 DoF model

The forces and moments were integrated in the wind axes as before, but the total airspeed, α, and β were adjusted to account for the magnitude and direction of wind gust disturbances (*Figure 20*).

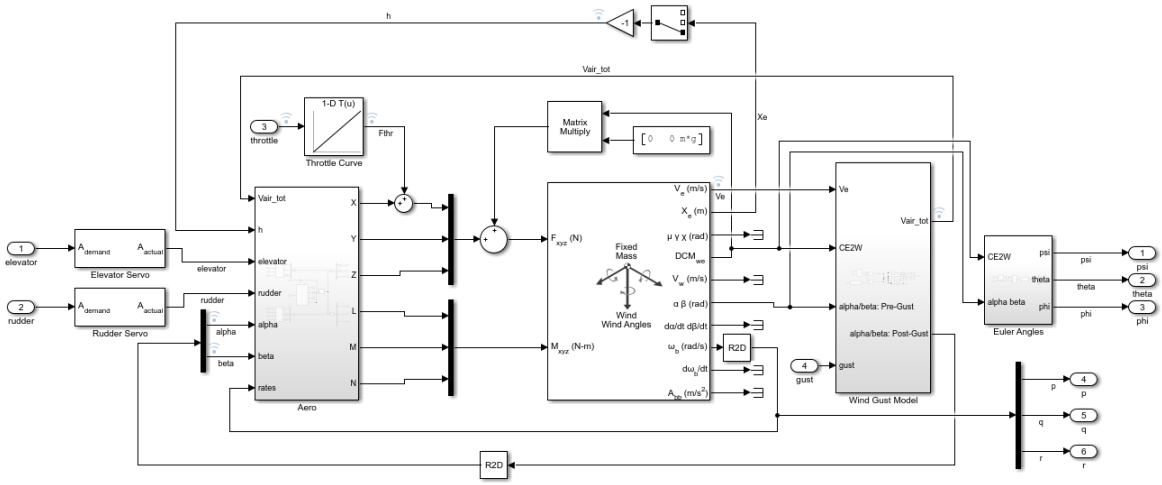

Figure 20: Integrating the equations of motion and adjusting α, β and total airspeed in the 6 DoF model.

The operating points from the 3 DoF model were also valid for the 6 DoF model because they did not incorporate rolling or yawing dynamics. An open-loop simulation of this model is shown in *Figures 21-22*.

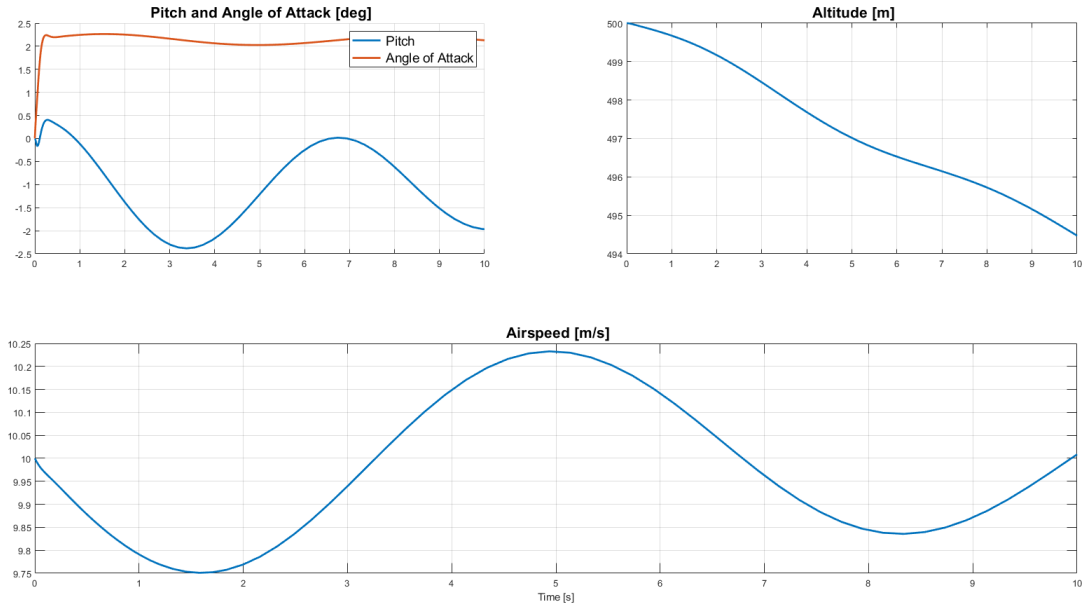

Figure 21: 6 DoF open-loop simulation of the longitudinal states.

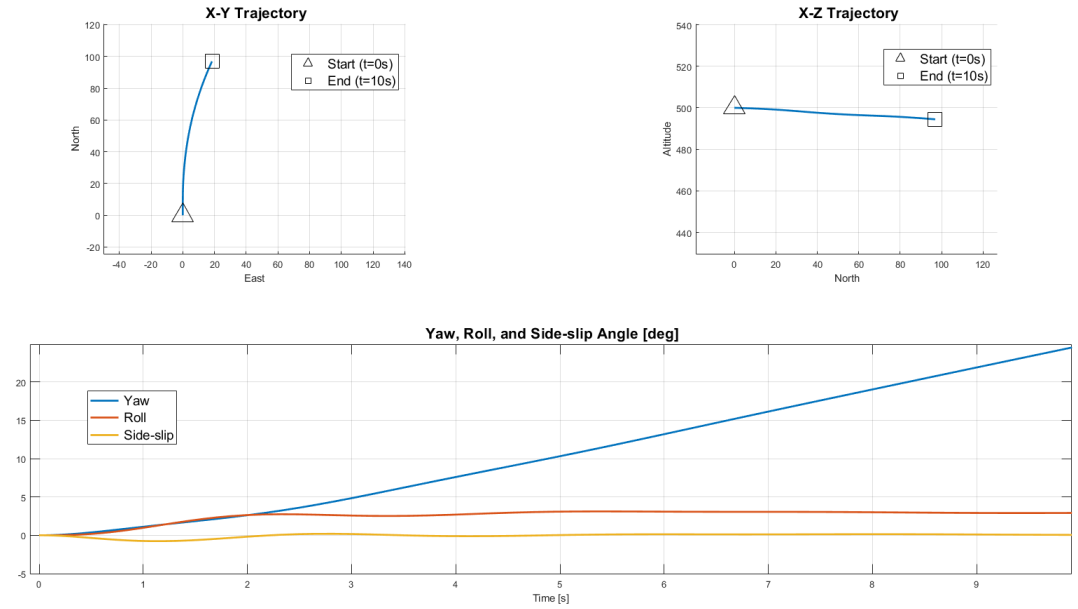

Figure 22: Trajectory and lateral Euler angles during a 6 DoF open-loop simulation. $\delta_r = 0.2^\circ$ to show roll and yaw dynamics.

The 6 DoF model was also stabilized with a set of cascading PID controllers. Since the roll and yaw dynamics are coupled, the lateral states can be stabilized using a single cascading controller. The goal roll angle and rudder deflection are determined by separate P controllers. The pitch controller was similar to the 3 DoF controller and works independently of the lateral PID controller. The structure of this controller is shown in *Figure 23*.

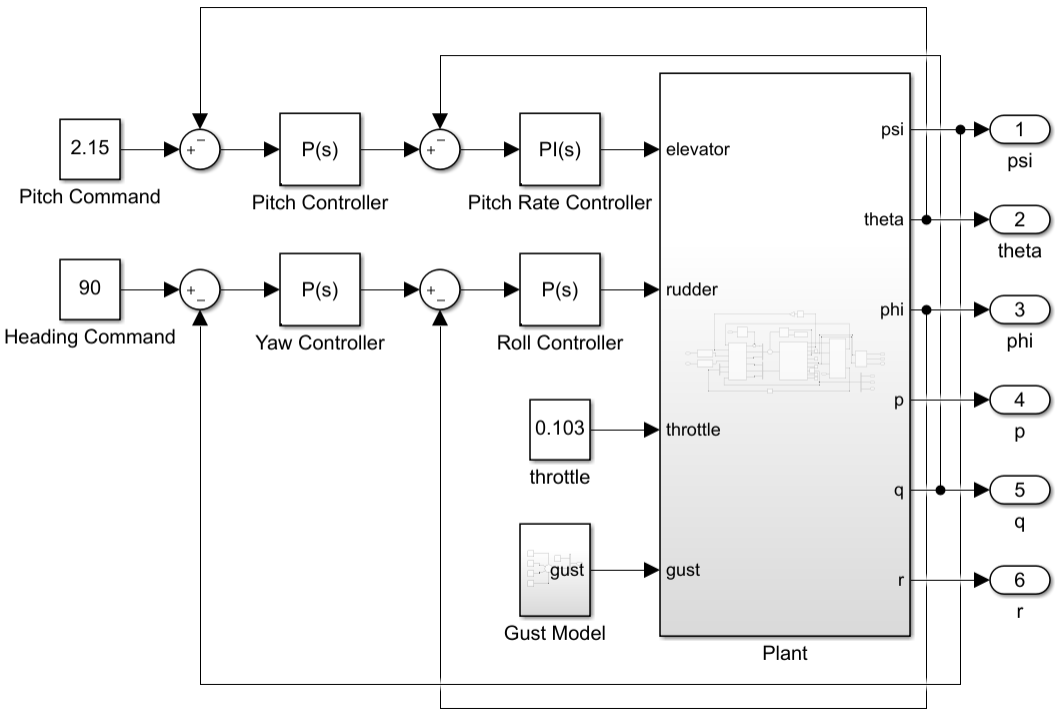

Figure 23: A set of cascading PID controllers for pitch and heading stabilization.

Figures 24-26 show the states of the aircraft tracking the operating point for steady level flight and a 60° heading using the PID controller over 20s. *Figures 27-29* show the same simulation with a $4m/s(\approx 9mph)$ gust disturbance blowing to the West starting at $t = 5s$ and lasting for 5s.

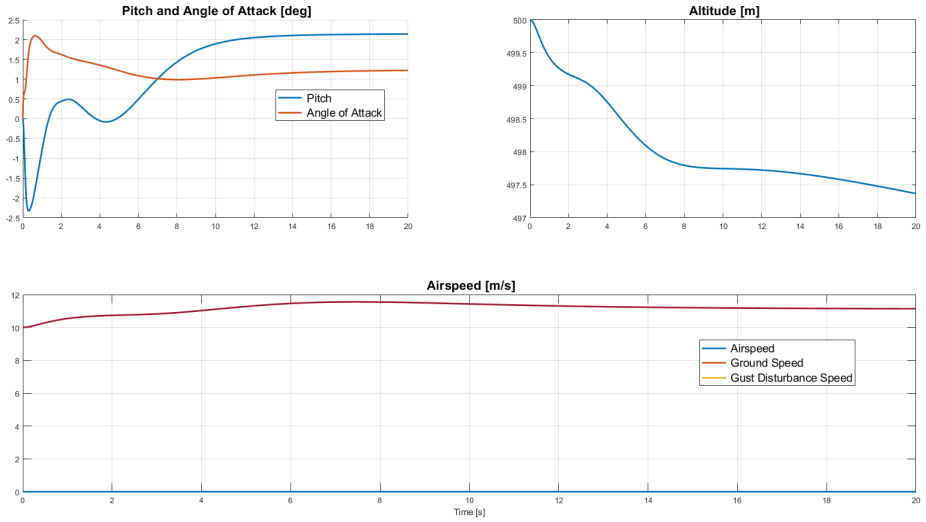

Figure 24: 6 DoF closed-loop simulation of the longitudinal states using a PID controller.

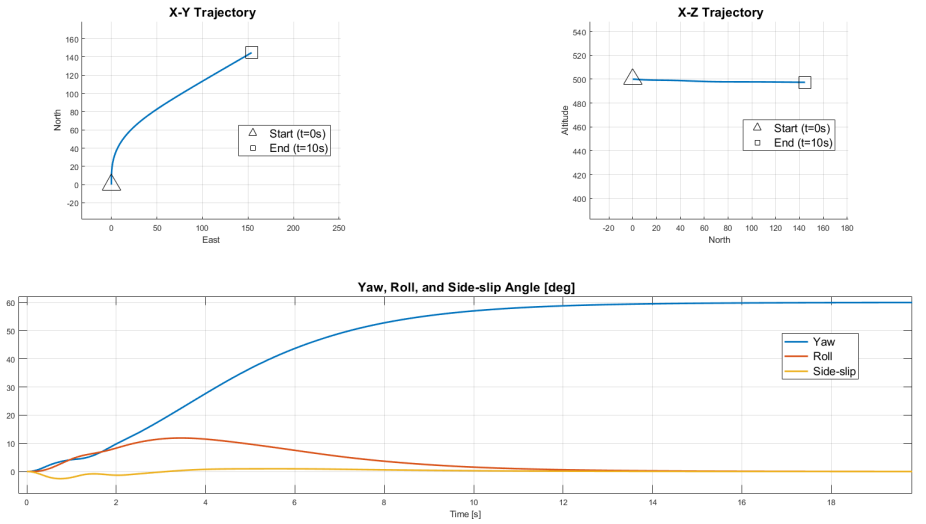

Figure 25: Trajectory of the 6 DoF model and lateral Euler angles stabilized using a PID controller.

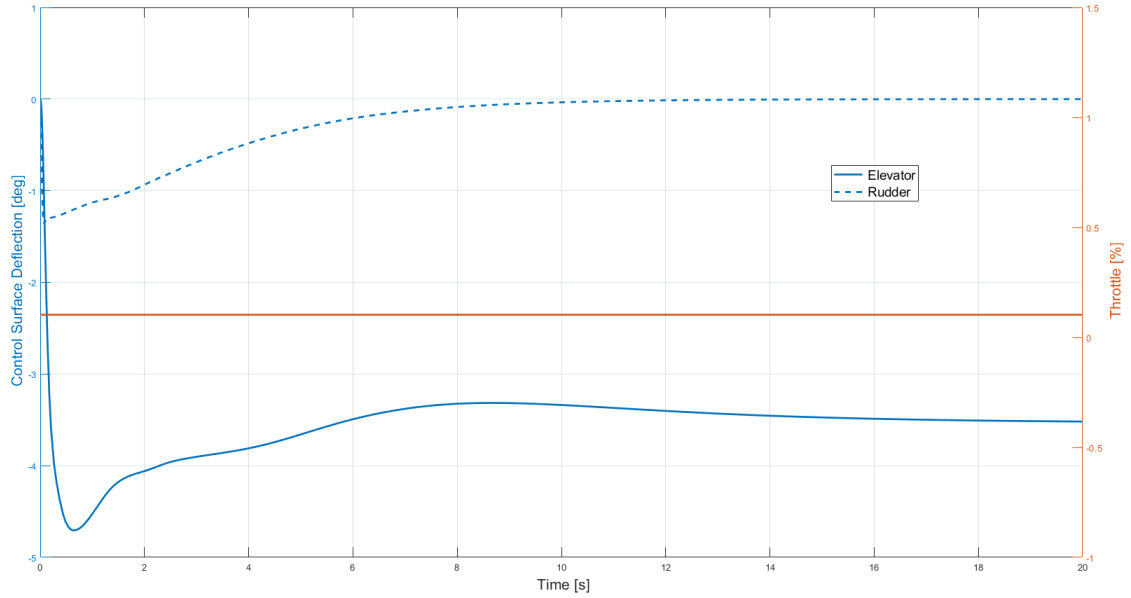

Figure 26: Control usage during the 6 DoF closed-loop simulation using a PID controller.

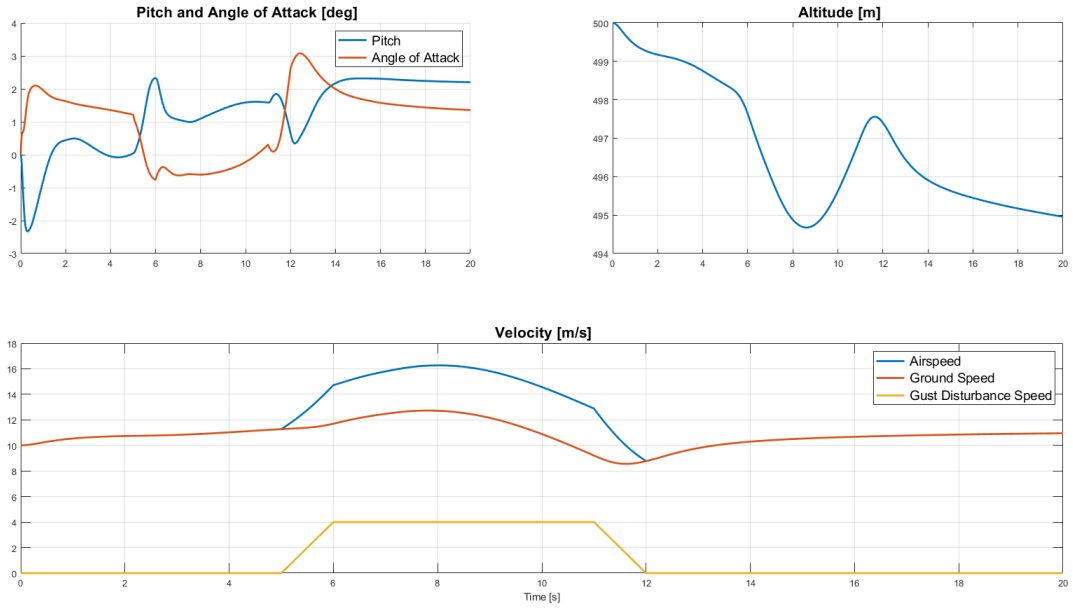

Figure 27: 6 DoF closed-loop simulation of the longitudinal states using a PID controller in the presence of disturbances.

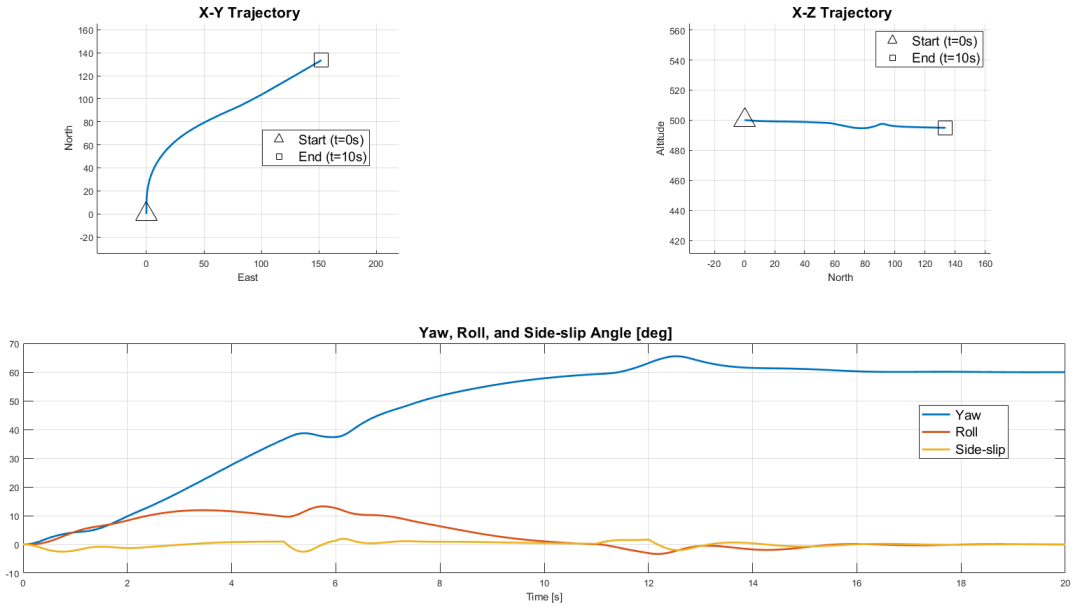

Figure 28: Trajectory of the 6 DoF model and lateral Euler angles stabilized using a PID controller in the presence of disturbances.

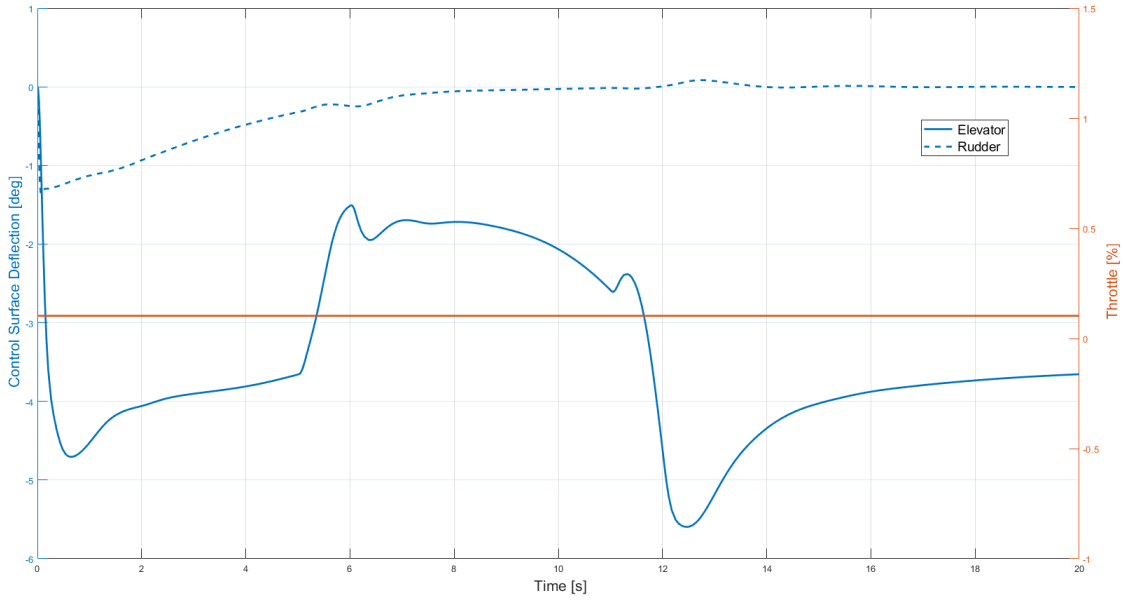

Figure 29: Control usage during the 6 DoF closed-loop simulation using a PID controller in the presence of disturbances.

Although this controller was simple to implement, it was difficult to tune as there are 3 parameters for each controller (12 in all). Additionally, there is no guarantee of optimality. These shortcomings of the PID controller were the motivation behind developing a Linear Quadratic Regulator (LQR) to stabilize the aircraft.

The LQR control law...

$$\tilde{\mathbf{u}} = -K\tilde{\mathbf{x}}$$

minimizes the quadratic cost function...

$$J = \int_0^\infty \tilde{\mathbf{x}}^T Q \tilde{\mathbf{x}} + \tilde{\mathbf{u}}^T R \tilde{\mathbf{u}} \ \ d\tau$$

constrained by the linearized dynamics of the system represented by...

$$\dot{\tilde{\mathbf{x}}} = A\tilde{\mathbf{x}} + B\tilde{\mathbf{u}}$$

$$\tilde{\mathbf{y}} = C\tilde{\mathbf{x}} + D\tilde{\mathbf{u}}$$

where $\tilde{\mathbf{x}} = \mathbf{x} - \mathbf{x}^* : \tilde{\mathbf{x}} \in \mathbb{R}^n$ represents the deviation of the state $\mathbf{x}$ from its operating point $\mathbf{x}^*$, $\tilde{\mathbf{u}} = \mathbf{u} - \mathbf{u}^* : \tilde{\mathbf{u}} \in \mathbb{R}^m$ represents the deviation of the control $\mathbf{u}$ from its operating point $\mathbf{u}^*$, and $\tilde{\mathbf{y}} = \mathbf{y} - \mathbf{y}^*$ represents the deviation of the output $\mathbf{y}$ from its operating point $\mathbf{y}^*$ [2] [7].

The optimal gain matrix K is found by solving for the solution S of the associated Riccati equation...

$$0 = A^T S + SA - SBR^{-1}B^T S + Q$$

$$K = R^{-1}B^T S$$

$Q \in \mathbb{R}^{n \times n}$ is a diagonal weighting matrix where *Q(i,i)* relates the cost J to the i^{th} state's deviation from its operating point. $R \in \mathbb{R}^{m \times m}$ is a similar weighting matrix relating the cost J to control usage.

Figures 30-35 show the same 6 DoF simulations as in *Figures 24-29*, except an LQR is used to stabilize the states.

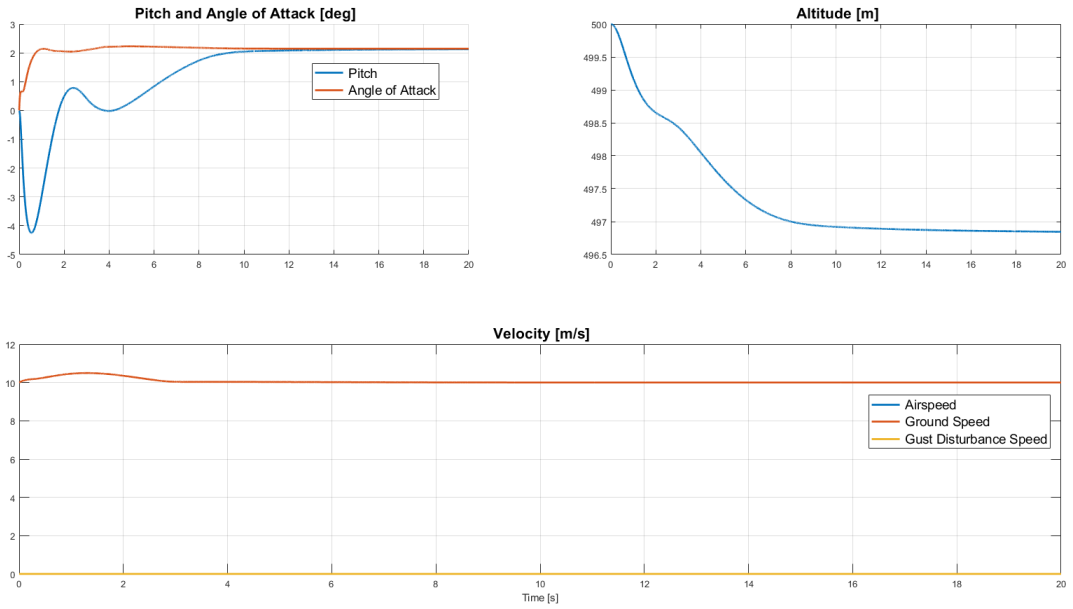

Figure 30: 6 DoF closed-loop simulation of the longitudinal states using an LQR controller.

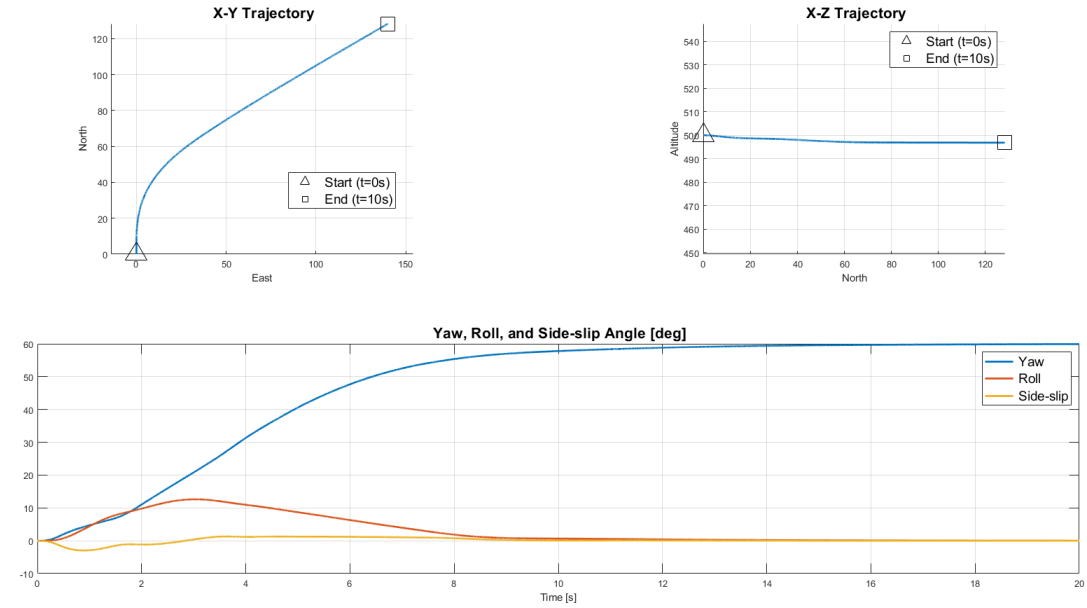

Figure 31: Trajectory of the 6 DoF model and lateral Euler angles stabilized using an LQR controller.

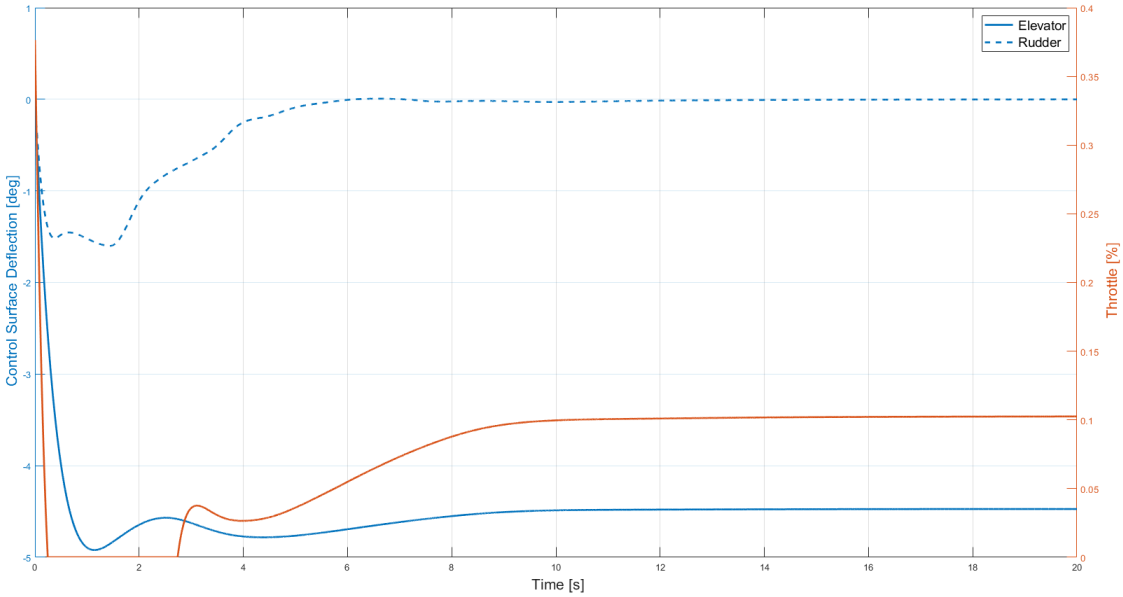

Figure 32: Control usage during the 6 DoF closed-loop simulation using an LQR controller.

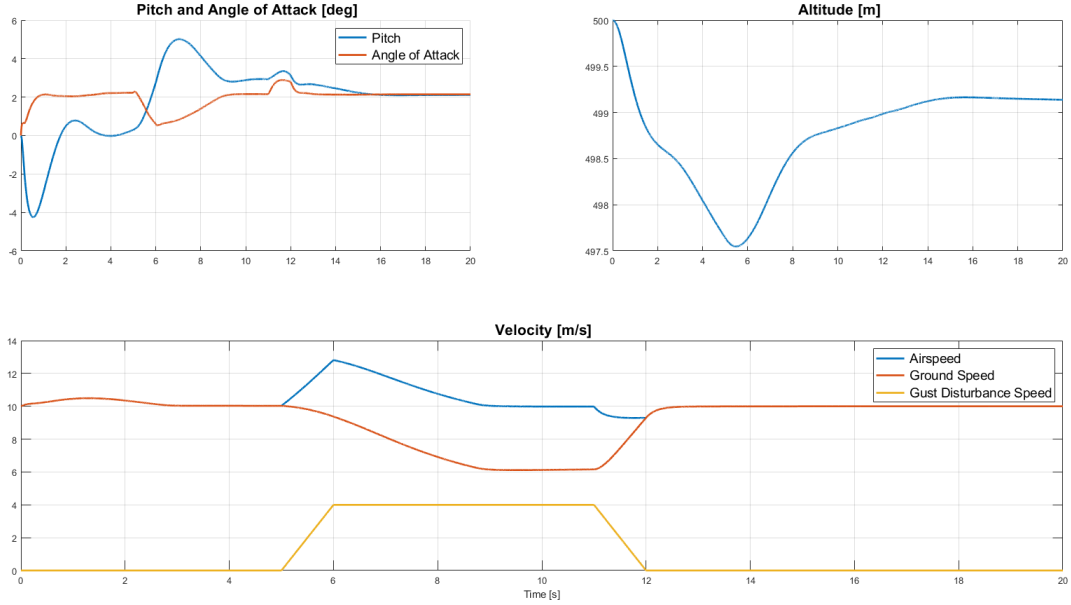

Figure 33: 6 DoF closed-loop simulation of the longitudinal states using an LQR controller in the presence of disturbances.

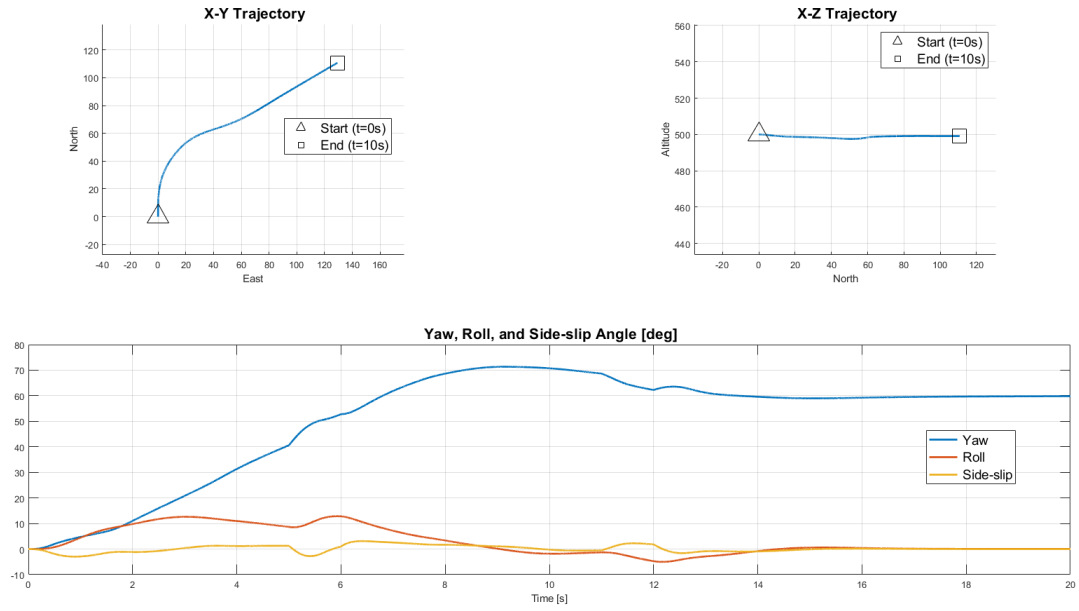

Figure 34: Trajectory of the 6 DoF model and lateral Euler angles stabilized using an LQR controller in the presence of disturbances.

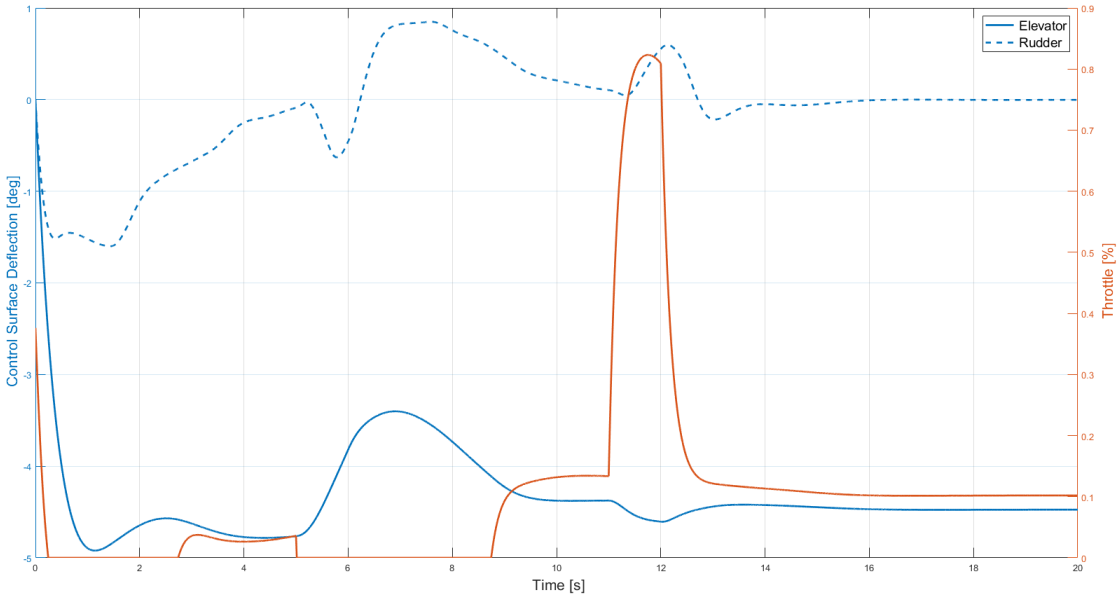

Figure 35: Control usage during the 6 DoF closed-loop simulation using an LQR controller in the presence of disturbances.

5 Validation of Simulated Results

The results of these simulations are consistent with expectations and don't violate assumptions in the analysis. For example...

- Angle of attack stays small (<10deg)
- model stays near its operating point (air density and viscosity are constant, airspeed stays close to its operating point of 10 m/s)

The intended actuator for a physical implementation of this model is a hobby servo connected to the control surface with a simple linkage. Data sheets for servo motors are available and were used to model the saturation limits of the actuator [14]. The modeled actuators have simulated saturation limits for the amount of control surface deflection *and* the rate of control surface deflection.

In addition, *XFLR5* solves for the frequency of the phugoid mode which can be compared to the frequency of the phugoid in the open loop trajectory of the *Simulink* model [12]. *Figure 36* shows the open-loop phugoid response of the 6 DoF model for 60 seconds.

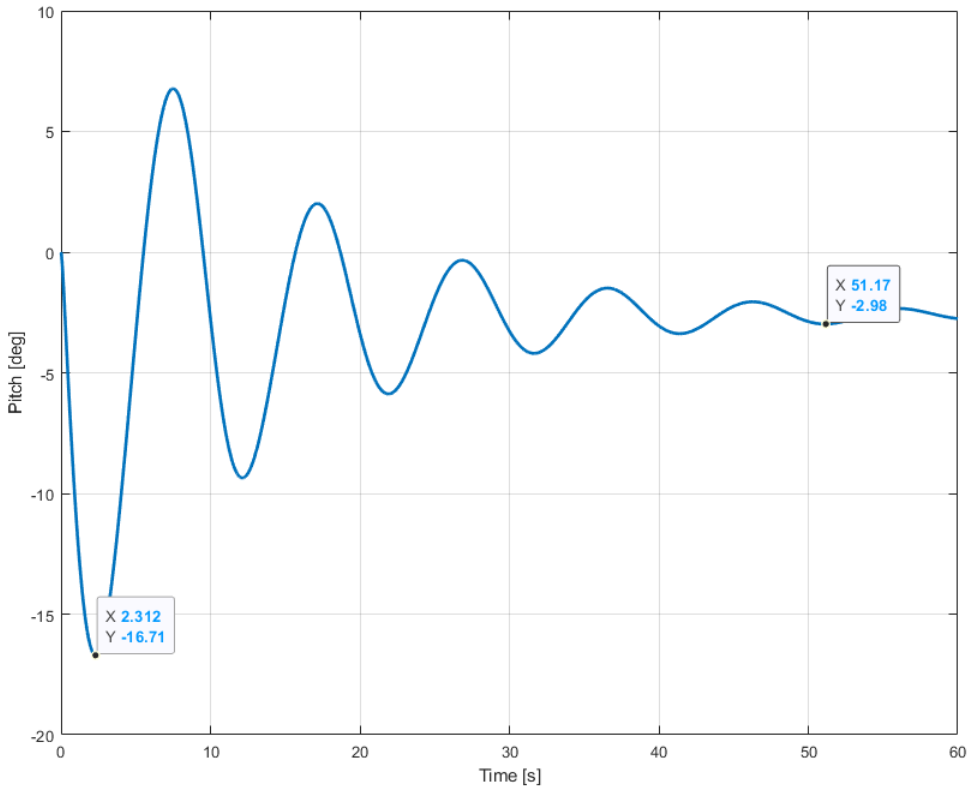

Figure 36: Phugoid response of the pitch over 60s

The period of the phugoid oscillations can be extracted from the response.

$$T_{Simulink} = \frac{51.2s - 2.31s}{5} = 9.78s$$

$$f_{XFLR5} = 0.082Hz, \;\; T_{XFLR5} = 12.1s$$

A 2.32s difference between the simulated phugoid periods indicate that each analysis agrees with each other.

6 Conclusion and Further Investigations

UAVs will prove to be an invaluable resource in the coming decades. This project has encompassed the basic modeling, simulation, and design principles necessary for working with complex industry platforms. Also, each simulation is generic enough to function with several designs of aircraft, provided that the geometry and aerodynamic coefficients are available. Careful planning and design went into how the simulations would fit together to produce a design tool with fast turnover.

This undertaking has produced satisfactory results as a design project, but implementing a physical system would incur its own set of challenges. For example, some issues are foreseen with ...

- Estimator dynamics (sensor noise, gimbal lock from Euler angles, prediction errors, etc.)
- Time delay from discretization and loop-time
- Violating the small α assumption
- Change in operating conditions (speed, temperature, air density, etc.)
- Non-stiff airframe/control linkages
- Non-symmetric airframe construction
- Air reaction moment from spinning a propeller will make banking one direction far easier than banking the other

Other interesting features to implement include ...

- Aileron/flaps model
- Estimator/measurement model
- Altitude/climb rate tracking
- Position tracking (circling)
- Takeoff/landing procedure

Although a physical system was beyond the scope of a semester project, there will certainly be further research and implementation in this field. In summary, an appreciable amount of experience has been developed concerning the analysis of aerospace dynamics and the design of heavier-than-air flying systems.

References

[1] Caughney, David A. Introduction to aircraft stability and control course notes for mae 5070, 2011.

[2] Ferrari, Silvia. Lecture notes from mae 6780: Multi-variable control theory, 2020.

[3] Han, Yang and Li, Peng and Ma, Jianjun and Wu, Wenqi. Adaptive dynamic surface control of flight with vector-coupled dynamics, 2019. [Online photo; accessed May, 2020].

[4] MacMartin, Douglas. Lecture notes from mae 4780: Feedback and control systems, 2019.

[5] MathWorks. Aerospace blockset, 2019. [Online; accessed January, 2020].

[6] MathWorks. Aerospace toolbox, 2019. [Online; accessed January, 2020].

[7] MathWorks. Design an lqr servo controller in simulink, 2020. [Online; accessed May, 2020].

[8] Mark Peters and Michael A. Konyak. The engineering analysis and design of the aircraft dynamics model for the faa target generation facility.

[9] Serra, Pedro. Image-based visual servo control of aerial vehicles, 2016. [Online photo; accessed May, 2020].

[10] Robert F. Stengel. *Flight Dynamics*. Princeton University Press.

[11] techwinder. Xflr5, an analysis tool for airfoils, wings and planes, 2020. [Online; accessed January, 2020].

[12] techwinder. Xflr5 and stability analysis, 2020. [Online; accessed February, 2020].

[13] Flite Test. Ft simple soarer speed build kit, 2020. [Online photo; accessed May, 2020].

[14] Tower Pro. *Micro Servo Motor*. [Online; accessed February, 2020].

[15] the free encyclopedia Wikipedia. Axes conventions, 2020. [Online photo; accessed May, 2020].